

X-ray holographic imaging of magnetic order in meander domain structures

Carlo Spezzani¹, Horia Popescu², Franck Fortuna³, Renaud Delaunay⁴, Marina Tortarolo², Nicolas Jaouen², Maurizio Sacchi^{2,5}

¹ELETTRA, Sincrotrone Trieste, Area Science Park, S.S.14, Km 163.5, 34012 Trieste, Italy

²Synchrotron SOLEIL, L'Orme des Merisiers, Saint-Aubin, B.P. 48, 91192 Gif-sur-Yvette, France

³Centre de Spectrométrie Nucléaire et Spectrométrie de Masse, Université Paris-Sud, Bât. 104, 91405 Orsay, France

⁴Laboratoire de Chimie Physique - Matière et Rayonnement, UPMC Paris 06, CNRS UMR 7614, 11 rue P. et M. Curie, 75005 Paris, France

⁵Institut des NanoSciences de Paris, UPMC Paris 06, CNRS UMR 7588, 4 Pl. Jussieu, 75015 Paris, France

Abstract. We performed x-ray holography experiments using synchrotron radiation. By analyzing the scattering of coherent circularly polarized x-rays tuned at the Co-2p resonance, we imaged perpendicular magnetic domains in a Co/Pd multilayer. We compare results obtained for continuous and laterally confined films.

1 Introduction

Perpendicular magnetic anisotropy (PMA) is one of the properties that are sought for when manufacturing artificially structured magnetic materials. A careful choice of the parameters makes it possible to prepare alloys or multilayer structures displaying PMA. In these systems, perpendicular magnetization is often accompanied by regular domain structures which display, at remanence, sub-micron characteristic length scales. These domain structures can be controlled, for instance, by applying an in-plane field or by varying the temperature. Knowledge of the response of the local magnetization to the action of a short magnetic pulse or of an ultra-fast local heating is of fundamental importance for envisaging applications. CoPd alloys and Co/Pd multilayers belong to this class of materials. In this paper we show how perpendicular magnetic domains in nanostructured Co/Pd multilayers can be imaged by a holographic technique based on resonant scattering of coherent soft x-rays.

2 X-ray imaging by Fourier-transform holography

Element selective imaging of the magnetization can be obtained by coherent scattering [1], a technique that takes advantage of all the most peculiar characteristics of synchrotron sources: high degree of coherence (for a large field of view), high flux (for collecting large angle

scattering) and short pulse duration (for time resolution). Imaging by Fourier transform holography (FTH) relies on the interference between coherent beams scattered by the object to be imaged and by a reference hole, whose size is the main limiting factor defining the overall spatial resolution [2]. When the sample is illuminated by a coherent wave-front, the spatial distribution of the optical constants within the object area generates a unique angular distribution of the scattered wave and this information is coded in phase and amplitude at the detector level, via the interference with the reference wave. The Fourier transform (FT) of the two-dimensional (2D) scattering diagram corresponds to the autocorrelation function of the entire sample (object and reference). By an appropriate sample design, the cross-correlation between object and reference can be well separated from the self-correlation of each one of them, providing an image of the object with a resolution limited primarily by the diameter of the reference hole [2]. For imaging magnetic domains, one tunes the photon energy at a core absorption resonance and relies on x-ray magnetic circular dichroism (XMCD) [3]: since the absorption coefficient (hence the optical index) depends on the sign of the magnetization, each given magnetic domain distribution within the object produces a specific diagram in coherent scattering. The object-reference cross-correlation in the 2D-FT of the scattering signal will image the magnetic domain structure as dark/bright areas, the intensity being related to the local projection of

the magnetization along the circular polarization vector of the incoming x-rays.

3 Experimental details

The most common approach to FTH (integrated mask/sample) has the sample, the object hole and the reference holes on one single membrane [2]. In our experiment, we used a different approach [4,5] where the sample and the holographic mask (object and reference holes) belong to two separate Si_3N_4 membranes. At the price of a more complex experimental set-up (the mask and the sample must be aligned with respect to each other and with respect to the beam), this approach offers the advantage of a much simpler sample and mask preparation. In particular, object and reference apertures of the holographic mask are through holes, making the focused ion beam (FIB) machining much simpler with respect to the integrated mask/sample design. An additional advantage, indispensable to our work, is that all areas of the sample can be imaged sequentially by a controlled relative displacement of the sample, something that would be impossible in the integrated sample/mask approach.

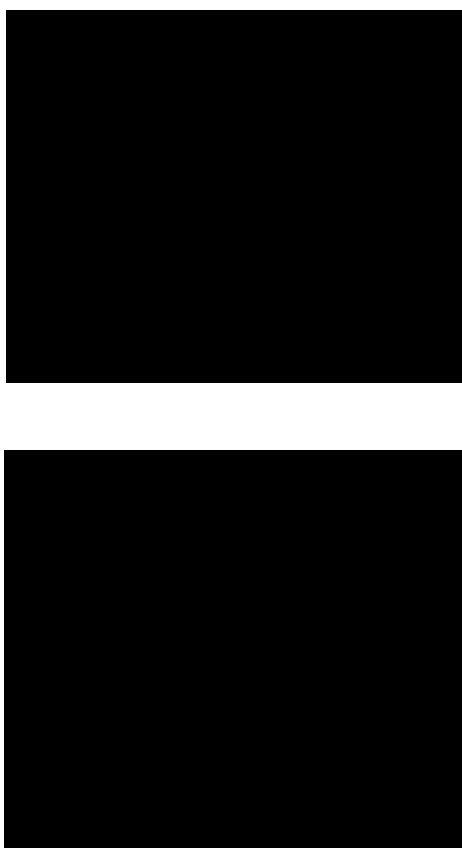


Fig. 1. SEM images of elements prepared by FIB milling. Top: holography mask with a 2 μm circular object aperture and three reference apertures. Bottom: patterned $(\text{Co}_{0.4}/\text{Pd}_{0.8})_{30}$ multilayer sample.

3.1. Sample preparation

$(\text{Co}_{0.4}/\text{Pd}_{0.8})_{30}$ multilayers were prepared by magnetron sputtering on 100 nm thick Si_3N_4 membranes (250!250 ! m² window in a 200 ! m thick Si frame). Two extra layers of Pd were used as buffer and protective layers. The samples, characterized by magneto-optical Kerr effect (MOKE) and by magnetic force microscopy (MFM), displayed strong perpendicular magnetic anisotropy and a meander domain structure with a magnetic period of about 130 nm. In-plane demagnetization cycles were applied prior to scattering experiments, favoring the parallel alignment of stripe domains.

3.2. Holography mask and FIB milling

Holography masks were obtained by FIB milling the object and reference through-holes in sputter-deposited x-ray opaque $(\text{Au}_{50\text{nm}}/\text{Cr}_{5\text{nm}})_{20}$ films on Si_3N_4 membranes. Object apertures (circular and square) ranged from 0.7 ! m to 3 ! m. Reference apertures (3 to 5 per mask, with nominal diameters from 50 nm to 120 nm) were placed at 2.5 object-diameters from the center of the object aperture, in order to guarantee that no overlap occurs in the 2D-FT between the object self-correlation and the object-reference cross-correlation. Laterally confined objects (squares and rectangles) were defined into the continuous Co/Pd film by FIB milling. Object size ranged from 300 nm to 2 μm , each element being isolated at the center of a 6 μm square where the Co/Pd multilayer had been removed. Examples of FIB milled holography mask and sample are given in Fig. 1.

3.3 X-ray beam characteristics

The experiment was carried out at the SEXTANTS beamline [6] of the SOLEIL synchrotron, using the IRMA-2 scattering chamber [7]. The beamline covers the 50-1700 eV energy range with full control of the x-rays polarization state. Resonant scattering measurements were performed at the Co L_3 edge (maximum absorption at 778 eV), using circular polarization. The use of both positive and negative helicities was essential for highlighting magnetic effects. In order to increase the transverse coherence of the x-ray beam, the angular acceptance of the beamline was limited to 40!40 μrad^2 using horizontal and vertical blades. Under these conditions, the transverse coherence length exceeds 20 μm in both directions [7].

3.4 Holography set-up

The holography mask was aligned with respect to the x-ray beam by two piezoelectric positioners. The sample was mounted on a three-axes translator driven by stepper motors, with encoded positioning. The contact between mask and sample surfaces was checked using a video-camera mounted outside the vacuum vessel. Both (Co/Pd) and (Au/Cr) layers were deposited on the side of the

Si₃N₄ membrane where the Si frame is located, therefore, by approaching their Si₃N₄ uncovered sides, we could bring them in close contact without risking any damage to the metallic films. A 2048!2048 13.5 μm pixel charge-coupled device (CCD) detector was mounted on a long-travel manipulator for adjusting its distance from the sample. In order to prevent visible stray light to reach the camera, a light-tight filter (Al-coated parylene) was mounted in front of the CCD. A 300 μm beamstop on a 10 μm thick wire placed just in front of the filter could be positioned via two piezoelectric motors, in order to block the intense transmitted beam.



Fig. 2. (a) Scattered intensity for right circularly polarized light and (b) difference between left and right polarization. The image size corresponds to $142 \mu\text{m}^{-1}$. (c) 2D-FT of (b), showing six cross-correlation images (three independent plus their conjugates) between the object aperture and three reference apertures. (d) Zoom on one cross-correlation image. The sample is a $2 \mu\text{m}$ square.

4 Results and discussion

Fig. 2a shows a scattering diagram collected using right circularly polarized x-rays tuned at the Co-L₃ absorption maximum (778 eV). Several features are worth noticing:

- i) The central spot (transmitted beam) is blocked by the beam-stop. This is essential for preserving dynamics in data collection, but it can make the FT analysis cumbersome.
- ii) Annular intense modulations correspond to the scattering from the round ($2 \mu\text{m}$) object hole defining the field of view (FOV).
- iii) Cross-shaped intensity corresponds to the scattering from a square element contained within the FOV.
- iv) Speckles at larger radii correspond to scattering from magnetic domains. Their position in reciprocal space ($\sim 50 \mu\text{m}^{-1}$) is directly related to the average magnetic period (130 nm).

v) Fine, very short period intensity modulations come from the interference with the wave scattered by the reference holes (three in this case).

By taking the difference between scattering diagrams recorded for opposite helicities of the x-rays, many features of Fig. 2a are washed out, giving preeminence to magnetic contributions (Fig. 2b). The 2D-FT of Fig. 2b produces the autocorrelation of the entire sample, including, in particular, the cross-correlation between object and reference apertures, leading to the image of Fig. 2c and 2d.

Similar data were recorded at different positions, corresponding to the continuous multilayer film and to two isolated objects (Fig. 3).

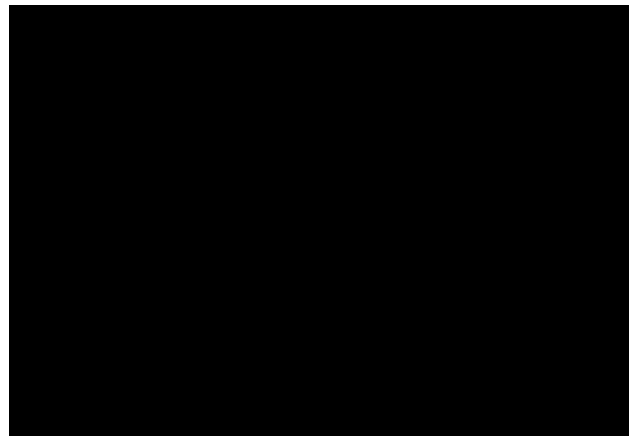


Fig. 3. Images of magnetic domains in the region of the continuous multilayer (a) and for two objects of size $2!2 \mu\text{m}^2$ (b) and $1.2!1.3 \mu\text{m}^2$ (c). Thick circles indicate the FOV, while thinner lines in (b) and (c) sketch the object borders.

For the continuous film, we observed a dominant parallel orientation of the perpendicular magnetic domains, with the stripes running along the in-plane demagnetization direction [8]. A few regions can be found which display discontinuities in the stripes organization, as shown in Fig. 3a, but overall the order is rather good and clear magnetic diffraction peaks can be observed in non-coherent scattering. The magnetic period is found to be 130 nm , in excellent agreement with MFM observations. This confirms also that, in terms of spatial resolution, we are close to the limit of $50\text{-}60 \text{ nm}$ set by the size of the reference apertures.

For the $2 \mu\text{m}$ square (Fig. 3b), up/down magnetization domains do not follow an ordered pattern in the object plane. The demagnetization direction is the same as in Fig. 3a, approximately along the square diagonal, but only a small fraction of the sample shows domains parallel to this direction. In the upper part of the object, stripes form mostly parallel to the side of the square, while on the left side it is hard to distinguish a clear pattern.

The image of a smaller object ($1.2!1.3 \mu\text{m}^2$ rectangle, Fig. 3c) shows even more clearly the tendency to lose the order of the stripes: domains retaining the original orientation as in the continuous film can be observed along the rectangle diagonal only, with a width that does

not exceed 500 nm. In the rest of the sample, no clear magnetic pattern can be outlined.

5 Conclusion

We have used x-ray holography for imaging perpendicular magnetic domains in a Co/Pd multilayer, comparing results obtained for the continuous film and for laterally confined objects. We are aware of the fact that, for these samples, similar results could have been obtained by other techniques, notably by MFM. Our work, though, aims at objectives of both immediate and long term interest. Producing images of perpendicular magnetic domains in nano-structured objects with ~50 nm spatial resolution is, if not unique, relevant in itself. With respect to other techniques, x-ray holography provides the element selectivity of core resonances, which, although inessential in our case, can be relevant for studying complex magnetic materials. Moreover, being based on x-ray transmission, FTH probes the entire thickness of the sample, another aspect that makes it complementary to MFM and to magnetic microscopy techniques based on visible light. On the long term, this kind of work allows us to acquire expertise in holographic x-ray imaging of small magnetic objects in the perspective of more complex applications, notably time-resolved imaging at fs-pulsed x-ray sources [9].

References

1. J.J. Turner, X. Huang, O. Krupin, K.A. Seu, D. Parks, S. Kevan, E. Lima, K. Kisslinger, I. McNulty, R. Gambino, S. Mangin, S. Roy, P. Fischer, *Phys. Rev. Lett.* **107**, 033904 (2011).
2. S. Eisebitt, J. Lüning, W. Schlotter, M. Lörger, O. Hellwig, W. Eberhardt, J. Stöhr, *Nature* **432**, 885 (2004).
3. P. Carra, B.T. Thole, M. Altarelli, X. Wang, "X-ray circular dichroism and local magnetic fields," *Phys. Rev. Lett.* **70**, 694 (1993).
4. D. Stickler, R. Frömter, H. Stillrich, C. Menk, C. Tieg, S. Streit-Nierobisch, M. Sprung, C. Gutt, L.M. Stadler, O. Leupold, G. Grübel, H.P. Oepen, *Appl. Phys. Lett.* **96**, 042501 (2010).
5. M. Sacchi, H. Popescu, N. Jaouen, M. Tortarolo, F. Fortuna, R. Delaunay, C. Spezzani, *Opt. Express* **20**, 9769 (2012).
6. M. Sacchi, N. Jaouen, H. Popescu, R. Gaudemer, F. Polack, B. Lagarde, G. Cauchon, A. Delmotte, J.M. Dubuisson, J.M. Tonnerre, G.S. Chiuzaiban, C.F. Hague, *Proceedings of the 11th International Conference on Synchrotron Radiation Instrumentation (SRI 2012)*, J. Phys. Conf. Series (to be published).
7. M. Sacchi, H. Popescu, R. Gaudemer, N. Jaouen, A. Avila, R. Delaunay, U. Maier, C. Spezzani, *Proceedings of the 11th International Conference on Synchrotron Radiation Instrumentation (SRI 2012)*, J. Phys. Conf. Series (to be published).
8. O. Hellwig, A. Berger, J.B. Kortright, E.E. Fullerton, *J. Mag. Mag. Mater.* **319**, **13** (2007).
9. T. Wang, D. Zhu, B. Wu, C. Graves, S. Schaffert, T. Rander, L. Müller, B. Vodungbo, C. Baumier, D.P. Bernstein, B. Braüer, V. Cros, S. deJong, R. Delaunay, A. Fognini, R. Kukreja, S. Lee, V. Lopéz-Flores, J. Mohanty, B. Pfau, H. Popescu, M. Sacchi, A.B. Sardinha, F. Sirotti, P. Zeitoun, M. Messerschmidt, J.J. Turner, W.F. Schlotter, O. Hellwig, R. Mattana, N. Jaouen, F. Fortuna, Y. Acremann, C. Gutt, H.A. Dürr, E. Beaurepaire, C. Boeglin, S. Eisebitt, G. Grübel, J. Lüning, J. Stöhr, A.O. Scherz, *Phys. Rev. Lett.* **108**, 267403 (2012).